Atomic Layer Deposition-Modified Bifunctional Electrocatalysts for Rechargeable Zinc-Air Batteries: Boosting Activity and Cycle Life

Fang Dong, Zhangsen Chen, Ning Chen, Gaixia Zhang, and Shuhui Sun**

The integration of transition metal-carbon composites has shown remarkable potential in achieving superior bifunctional electrocatalytic activity and robust stability in rechargeable zinc-air batteries (ZABs), primarily through electronic structure modulation and strategic structural design. While significant research is dedicated to the initial structure and performance of bifunctional electrocatalysts for rechargeable ZABs, their dynamic evolution during charge–discharge cycling remains underexplored. In this study, CoFe nanoparticles are encapsulated within carbon nanotubes co-doped with nitrogen and phosphorus (NPC) to mitigate dissolution and erosion risks. Further, the catalyst surface (CoFe-NPC) is precisely modified with a thin layer of nickel oxide (NiO) via atomic layer deposition (ALD), forming a protective layer with catalytic activity. The resulting ALD-modified catalyst, CoFe-NPC@NiO, exhibits outstanding bifunctional performance ($\Delta E = 0.592$ V) for the oxygen reduction reaction (ORR) and oxygen evolution reaction (OER). Notably, the liquid flow ZAB using the CoFe-NPC@NiO cathode demonstrates exceptional rechargeable stability (2700 h, ≈4 months). Theoretical calculations and in situ X-ray absorption spectroscopy (XAS) analyses reveal that NiO modification significantly enhances both the catalytic activity and stability of the electrocatalyst. This work will provide valuable insights into the design of advanced electrocatalysts, facilitating advancements in activity enhancement, stability improvement, and selectivity optimization.

1. Introduction

To address the escalating challenges of air pollution and growing global energy demands, the advancement of clean energy conversion and storage technologies has garnered significant attention. Rechargeable zinc-air batteries (ZABs) are poised to emerge as one of the most promising electrochemical energy storage devices owing to their inherent advantages of high energy density, cost-effectiveness, intrinsic safety, and eco-friendliness.[1] However, the sluggish kinetics and limited reversibility of the oxygen reduction reaction (ORR) and oxygen evolution reaction (OER) at the air cathode remain critical challenges, hindering the achievement of extended battery lifespan and optimal charge/discharge efficiency.[2]

Precious metal catalysts, such as Pt-based catalysts for the ORR and Ir/Ru-based catalysts for the OER, are widely acknowledged for their outstanding catalytic activity and stability.[3] However, their high cost, limited availability, and insufficient bifunctional performance remain significant obstacles to the commercial adoption of ZABs.[4] Both ORR and OER are reversible reactions characterized by high overpotentials, necessitating catalysts with distinct active components for each reaction. Furthermore, ORR catalysts are susceptible to oxidation under the high oxidative conditions present during the OER process, leading to a decline in activity. The development of composite structures that integrate multiple catalytic components has emerged as a promising strategy to enable efficient bifunctional catalysis.[5]

Composite materials that integrate transition metals with carbon materials have demonstrated significant potential in improving both ORR and OER electrocatalytic activity, as well as enhancing stability through electronic structure modulation and rational structural design.[6] Achieving continuous and efficient energy conversion in ZABs necessitates bifunctional catalysts with robust activity and stability throughout the charge-discharge cycles. However, electrocatalysts often undergo surface reconstruction, structural evolution, and active site transformation, which can either lead to the formation of more stable active sites or result in performance degradation due to the loss or passivation of active components.[7] Additionally, carbon-based substrates are

F. Dong, Z. Chen, S. Sun
Institut National de la Recherche Scientifique (INRS)
Center Énergie Matériaux Télécommunications
Varennes, Québec J3X 1P7, Canada
E-mail: shuhui.sun@inrs.ca

N. Chen
Canadian Light Source (CLS)
Saskatoon, SK S7N 2V3, Canada

G. Zhang
Department of Electrical Engineering
École de Technologie Supérieure (ÉTS)
Montréal, Québec H3C 1K3, Canada
E-mail: gaixia.zhang@etsmtl.ca

The ORCID identification number(s) for the author(s) of this article can be found under https://doi.org/10.1002/aenm.202502074

DOI: 10.1002/aenm.202502074

susceptible to corrosion in electrolytic environments, which can reduce their surface area and cause the shedding or agglomeration of active materials. The electrochemical corrosion during the OER process further compromises the overall electrocatalytic efficiency.[8] To overcome these challenges, the corrosion resistance of carbon materials can be improved by developing high-graphitized carbon structures, such as graphene or carbon nanotubes (CNTs), through high-temperature treatment or by utilizing pre-existing high-graphitized carbon materials.[9] Incorporating graphitic nitrogen dopants has also proven effective in improving the durability of carbon materials.[10] Beyond doping and alloying, synergistic strategies leveraging interfacial interactions among different components have been employed to enhance the corrosion resistance of electrocatalysts.[11] Additionally, protective shell coatings on electrocatalysts have shown promise in mitigating the dissolution and inactivation of active components by the electrolyte. To maximize performance, such protective shells must possess optimal electrical conductivity, appropriate thickness, and excellent corrosion resistance, ensuring adequate exposure of active sites as well as efficient electron and mass transport.[12]

Atomic layer deposition (ALD) is highly attractive for energy storage devices due to its precise control over composition and thickness, exceptional uniformity, and ability to produce conformal, thin-film coatings with remarkable consistency.[13] Recent studies have demonstrated that ALD coatings applied as protective layers on cathode materials significantly improve the cyclic stability of lithium-ion and sodium-ion batteries.[14] In addition to enhancing catalyst stability through the formation of ultra-thin, uniformly structured coatings, ALD also preserves the structural and morphological integrity, as well as the intrinsic properties, of the materials.[15] More interestingly, the ability of ALD to effectively customize catalytic properties enables the design of complex and innovative nanostructures, offering a pathway to further improve overall catalytic efficiency.[16]

Recently, we developed bimetallic heterostructures encapsulated within N/P-doped CNTs as highly efficient bifunctional electrocatalysts for rechargeable ZABs.[17] On the one hand, CNTs can effectively prevent the migration and corrosion of encapsulated nanoparticles, thereby improving long-term stability. On the other hand, CNTs can transfer electrons from transition metal nanoparticles to the outer surface for distribution and activation as active sites. However, carbon materials will inevitably undergo carbon corrosion and dissolution of active substances in the harsh electrochemical environment, leading to a decrease in catalyst activity. To ensure the long-term durability of the battery, a uniform, and robust film can be employed as a protective layer. By optimizing the composition and thickness of the ALD-modified transition metal oxide films, an optimal balance between ORR and OER activity was achieved. The resulting catalyst CoFe-NPC@NiO-10 exhibited exceptional bifunctional activity ($\Delta E = 0.592$ V). More importantly, in situ reconstruction of the transition metal during charge and discharge was observed, providing insights into the actual active sites of the catalyst in ZABs. As a result, the CoFe-NPC@NiO-based ZAB demonstrated an impressive power density of 607.1 mW cm^{-2} and remarkable long-term stability, maintaining performance for up to 2700 h at a current density of 5 mA cm^{-2}.

2. Results and Discussion

Using bimetallic heterostructures encapsulated within N/P-doped CNTs as the base catalyst, a series of ALD-modified bifunctional catalysts were synthesized by depositing a thin and uniform coating on the surface via ALD, as illustrated in **Figure 1**a. To investigate the morphology and microstructure of the carbon nanotube composite structure, field-emission scanning electron microscopy (SEM) and transmission electron microscopy (TEM) were employed for morphological characterization and elemental analysis. Low-magnification SEM images (Figure 1b; Figure S1, Supporting Information) reveal that the catalyst comprises uniformly intertwined CNTs with lengths spanning several micrometers and diameters ranging from tens to hundreds of nanometers. High-magnification SEM images (Figure 1c) indicate that the hollow tubular structure of the CNTs remains largely intact, suggesting that the NiO thin film deposited via ALD does not significantly alter their morphology. TEM images provide detailed information on the structural relationships between the catalyst components. Metal nanoparticles are observed to adhere to the openings and interiors of the CNTs (Figure 1d). However, lattice patterns characteristic of NiO are not observed, possibly due to the ultra-thin nature of the NiO coating introduced by ALD (Figure 1e; Figure S4, Supporting Information). Energy-dispersive X-ray (EDX) mapping confirms the elemental distribution, showing the presence of Co, Fe, and P concentrated within the nanoparticles (Figure 1f), while C, N, and P are uniformly distributed on the CNT surfaces (Figure 1g). EDS mapping of O and Ni further verifies the successful deposition of the NiO coating, which avoids aggregation. This ultra-thin coating preserves the structural integrity of the CNTs and maintains their inherent electrical conductivity. In contrast, the morphology of NiFe-NPC@NiO shows significantly fewer CNTs compared to CoFe-NPC@NiO (Figure S2, Supporting Information). For NiFe-NPC@NiO, the nanoparticles are not encapsulated within the CNTs but instead adhere to their surfaces and interweave among the tubes (Figure S5, Supporting Information). Meanwhile, FeFe-NPC@NiO exhibits a distinct morphology. Although a few underdeveloped CNTs are visible in magnified SEM (Figure S3, Supporting Information) and TEM images (Figure S6, Supporting Information), the overall structure more closely resembles porous carbon materials characterized by dense and heterogeneous voids.

Nitrogen (N_2) adsorption-desorption isotherms were measured to analyze the surface area and pore structure of various catalysts, with a focus on understanding the effect of ALD cycles on catalyst morphology and pore size distribution. The low-pressure region of the isotherms exhibited pronounced adsorption, indicating a substantial presence of micropores. In the intermediate pressure region, a characteristic type IV curve with adsorption-desorption hysteresis is observed, suggesting well-developed mesoporous structures (**Figure 2**a; Figures S7 and S8, Supporting Information).[18] The specific surface areas of CoFe-NPC@NiO, NiFe-NPC@NiO, and FeFe-NPC@NiO were calculated to be 290.73, 260.36, and 198.71 m^2 g^{-1},

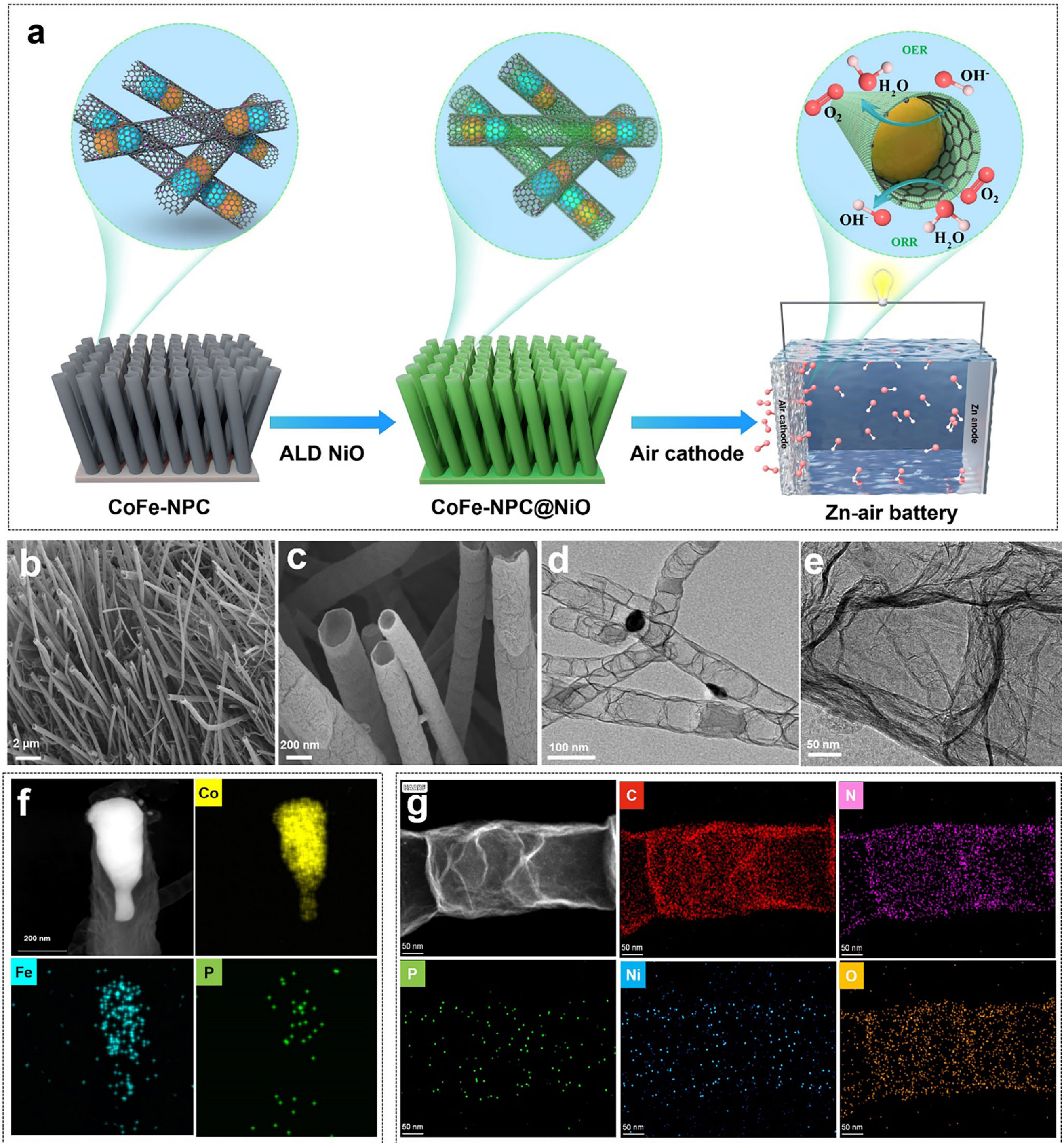

Figure 1. a) Schematic illustration of the ALD-modified bifunctional catalyst design for ZABs. b,c) SEM images, d,e) TEM images, and f,g) EDS elemental mapping of CoFe-NPC@NiO.

respectively, reflecting differences in the structural development of the CNTs. As shown in Figure 2d, the specific surface area of CoFe-NPC@NiO-10 (290.73 m^2 g^{-1}) is higher than that of CoFe-NPC@NiO-40 (260.10 m^2 g^{-1}), but lower than that of CoFe-NPC (309.30 m^2 g^{-1}), indicating a significant reduction in surface area with increasing ALD cycles. This conclusion is further supported by the decrease in the specific surface area of CNT@NiO (253.07 m^2 g^{-1}) compared to the pristine CNTs (284.79 m^2 g^{-1}) (Figure S9, Supporting Information). The pore size distribution curve reveals the presence of both micropores and mesopores in all catalysts. In contrast, NiFe-NPC@NiO and FeFe-NPC@NiO display dominant peaks in the mesoporous region

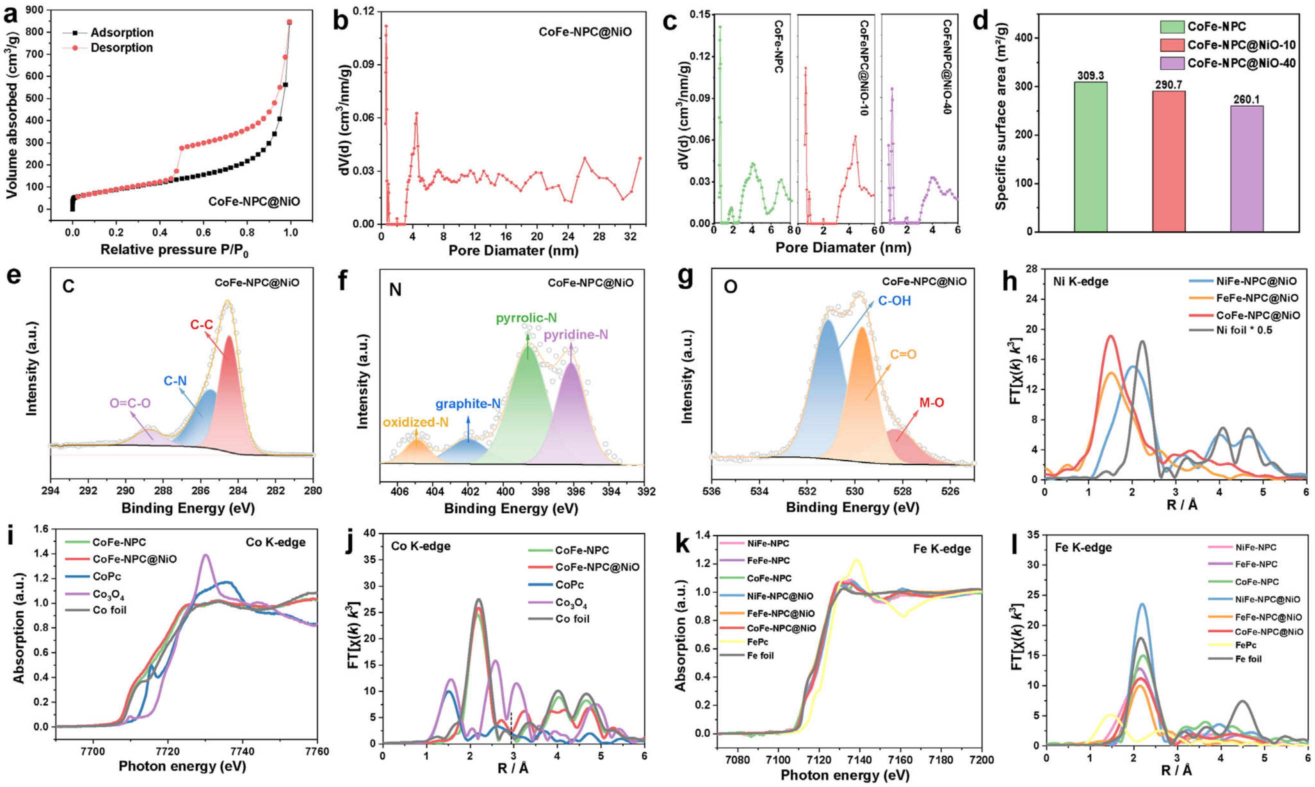

Figure 2. a) N_2 adsorption-desorption isotherm and b) the corresponding pore size distribution curve of CoFe-NPC@NiO-10. c) Pore size distribution and d) BET surface areas of CoFe-NPC, CoFe-NPC@NiO-10, and CoFe-NPC@NiO-40. XPS spectra of e) C 1s, f) N 1s, and g) O 1s for CoFe-NPC@NiO-10. h) Ni K-edge Fourier transforms of the k^3-weighted EXAFS spectra for different catalysts. i) Normalized Co K-edge XANES spectra and k) Fe K-edge XANES spectra, and the corresponding j) Co K-edge and l) Fe K-edge Fourier transforms of the k^3-weighted EXAFS spectra for the prepared and reference catalysts.

(Figure S7e,f, Supporting Information), while CoFe-NPC@NiO exhibits a peak at around 0.6 nm (Figure 2b), indicating a higher abundance of micropores. This suggests that as the ALD cycle number increases, micropores gradually diminish, while the number of mesoporous pores initially increases and then decreases (Figure 2c; Table S1, Supporting Information). This transformation is likely due to the conversion of macropores into mesopores by the ALD membrane, followed by the obstruction of micropores as the coating thickness increases. Excessively thick ALD coatings result in pore annihilation and a corresponding decrease in specific surface area. The high microporosity of micropores contributes significantly to the catalytic activity by providing abundant accessible active sites for catalytic reactions. Simultaneously, the presence of well-developed mesoporous pores reduces mass transfer resistance and facilitates electron and ion transport, enhancing the overall catalytic performance.[19]

The non-metallic chemical composition and bonding states of CoFe-NPC@NiO were analyzed using X-ray photoelectron spectroscopy (XPS), focusing on the elements C, N, and O. The high-resolution C 1s spectrum was deconvoluted into three distinct peaks at binding energies of 284.5, 285.3, and 288.8 eV, corresponding to C—C, C—N, and O═C—O bonds, respectively (Figure 2e). The detection of C—N bonds confirms the successful incorporation of nitrogen into the carbon framework. The high-resolution N 1s spectrum of CoFe-NPC@NiO reveals four nitrogen species, with peaks at binding energies of 396.2, 398.6, 401.9, and 405.0 eV, corresponding to pyridinic nitrogen, pyrrolic nitrogen, graphitic nitrogen, and oxidized nitrogen, respectively (Figure 2f). Pyridinic nitrogen is critical for modulating the local electronic structure, accelerating electron transfer, and enhancing catalytic activity.[20] Additionally, high content of graphitic nitrogen improves electronic conductivity and facilitates electron transfer on adjacent sp^2-hybridized carbons, enhancing reaction kinetics and corrosion resistance of the carbon material.[21] The M—O peak observed in Figure 2g confirms the successful surface modification of CNTs achieved via ALD. The crystal structures of CoFe-NPC and CoFe-NPC@NiO were analyzed using X-ray diffraction (XRD). The results revealed only the characteristic diffraction peaks of metallic Co, with no distinct peaks corresponding to metal oxides or metal phosphides detected. This absence could be attributed to the detection limitations of XRD (Figure S10, Supporting Information).

To gain a deeper comprehension of the intricate details of the local electronic structure and coordination environment of metal species in the catalyst, measurements were conducted employing normalized synchrotron X-ray absorption near edge structure (XANES) and Fourier transformed k^3-weighted extended X-ray absorption fine structure (EXAFS) spectroscopy. The Ni K-edge Fourier transforms of the k^3-weighted EXAFS spectra for FeFe-NPC@NiO and CoFe-NPC@NiO exhibit distinct peak features at 1.50 Å, which can be attributed to the Ni-O bonding environment (Figure 2h). Furthermore, the Ni K-edge of the EXAFS spectra of NiFe-NPC@NiO shows a more pronounced leftward shift compared to Ni foil (2.23 Å). This shift not only confirms the presence of metallic Ni but also suggests the formation of Ni-O bonds with shorter bond lengths, further supporting the formation of nickel oxide. As shown in Figure 2i, the Co K-edge spectra for both CoFe-NPC and CoFe-NPC@NiO show a pre-edge hump similar to the Co foil edge at 7712 eV, which corresponds to the electronic transition from 1s to 3d orbitals.[7b] The absorption edge and the main absorption peak of CoFe-NPC and CoFe-NPC@NiO are very close to those of Co foil. The Fe K-edge XANES spectra reveal that the majority of the synthesized catalysts exhibit slightly weakened pre-edge peaks, with the exception being that the FeFe-NPC@NiO and Fe foil curves nearly coincide (Figure 2k). The absorption edges of these samples are located between Fe foil and FePc, indicating that the Fe species in the catalysts exhibit oxidation states ranging from 0 to +4. Specifically, Fe atoms in CoFe-NPC and CoFe-NPC@NiO show lower oxidation states compared to NiFe-NPC and NiFe-NPC@NiO, as evidenced by the absorption edge shifting to lower energies.[22] The electrocatalytic activity correlates strongly with the local and electronic structures of different metals in the catalyst.[23] In the EXAFS Fourier-transform spectra (Figure 2j,l), both CoFe-NPC and CoFe-NPC@NiO display a prominent peak around 2.18 Å, attributed to Co—M and Fe—M scattering paths in the Co and Fe K-edges, respectively. However, the EXAFS spectra of the CoFe-NPC show leftward and rightward shifts in the positions of the Co—M and Fe—M peaks relative to Co foil and Fe foil respectively, providing strong evidence for Fe–Co bonding. Additionally, peaks corresponding to Co/Fe—N and Co/Fe—O are not observed in either catalyst. The doping of transition metals may lead to the formation of multiple active sites directly or influence morphology by increasing edge and defect density, which may enhance the density and accessibility of active sites.[24]

To evaluate the ORR performance of the prepared electrocatalyst, the prepared catalyst and commercial Pt/C were tested using a three-electrode system in the N_2 or O_2-saturated 0.1 M KOH at room temperature. To obtain protective films with effective catalytic active ingredients, various metal oxides were deposited on CoFe-NPC as a base catalyst via ALD. Ni, Co, and Ti were selected as candidates for synthesizing ALD-modified catalysts under identical experimental conditions. Among the modified catalysts, both CoFe-NPC@NiO and CoFe-NPC@CoO exhibit significant oxygen reduction peaks under oxygen-saturated conditions, whereas CoFe-NPC@TiO did not show noticeable activity. Linear sweep voltammetry (LSV) polarization curves for both ORR and OER, along with electrochemical impedance spectroscopy (EIS) measurements, were performed on the base catalyst and ALD-modified variants. The results confirm that the introduction of ALD-modified NiO on the catalyst surface enhances both ORR and OER activities while maintaining charge transfer impedance at the same level as the base catalyst (Figures S11 and S12, Supporting Information). This leads us to further explore the universality of NiO's effect on other catalysts and its influence on their activity and long-term durability.

According to the cyclic voltammetry (CV) curve in **Figure 3**a, all catalysts exhibit distinct peaks in the O_2-saturated electrolyte compared to the N_2-saturated electrolyte. Remarkably, CoFe-NPC@NiO shows an oxygen reduction peak at a more positive potential than the other catalysts, suggesting superior ORR activity. The ORR activity was further evaluated using LSV at a rotation speed of 1600 rpm (Figure 3b; Figure S13, Supporting Information). Among the unmodified NiO catalysts, FeFe-NPC shows the most positive ORR with a half-wave potential ($E_{1/2}$) of 0.901 V, comparable to commercial Pt/C and higher than CoFe-NPC (0.887 V) and NiFe-NPC (0.832 V). However, ALD modification has varying effects on the ORR activity of these catalysts. Specifically, ALD modification favors the catalyst CoFe-NPC to achieve an optimal ORR catalytic activity of 0.905 V. Conversely, NiO films have negligible impact on NiFe-NPC (0.83 V), while it significantly reduces the catalytic activity of FeFe-NPC to 0.879 V. The OER catalytic performance of all samples in a 1 M KOH solution is illustrated in Figure 3c and Figure S12b,e (Supporting Information). It is revealed that the CoFe-NPC@NiO catalyst exhibits the most superior OER performance among them, surpassing other catalysts and even outshining commercial RuO_2. The catalyst before ALD modification is intriguingly noteworthy, as the FeFe-NPC exhibits unparalleled ORR activity while paradoxically displaying the poorest OER performance. This indicates that the active sites in FeFe-NPC were insufficient to support bifunctional activity. Unlike its effect on ORR, the ALD-modified NiO films significantly enhance the OER performance of both CoFe-NPC and FeFe-NPC. Their OER potential at 10 mA cm^{-2} (E_{10}) experiences a reduction from 1.557 and 1.652 V to 1.493 and 1.596 V respectively, reflecting impressive improvements in OER efficiency. Conversely, the NiFe-NPC catalyst exhibits hindered OER performance after ALD modification, as evidenced by an increase in E_{10} from 1.589 to 1.649 V. The OER reaction kinetics was further evaluated by EIS. According to the Nyquist curve and impedance fitting data presented in Figure 3d, it is found that CoFe-NPC@NiO displays the smallest interfacial charge transfer resistance, indicating that it has faster charge transfer capability and superior electrochemical performance.

The variations in thickness and composition of ALD coatings play a critical role in determining their effectiveness in enhancing and stabilizing catalytic activity.[25] The coating thickness can be precisely tailored with atomic-precision control by adjusting the number of ALD cycles. The ALD coating must be sufficiently thick to provide chemical resistance and stability. However, an excessively thick coating leads to an increase in charge transfer resistance and mass transport resistance. Additionally, the porosity of the coating may hinder the effective exposure of active components within the coating through a constraint effect, consequently leading to a loss of catalytic activity.[25,26] Therefore, precise control of the ALD coating thickness is crucial for achieving an optimal balance between high catalytic activity and stability. We optimized the thickness of the NiO coating to achieve the catalyst with optimal bifunctional activity. The impact of various ALD cycles (2, 5, 10, 20, and 40) on the ORR and OER properties of CoFe-NPC@NiO catalyst were investigated (Figures S14 and S15, Supporting Information). As depicted in Figure 3i, upon summarizing and comparing the ORR $E_{1/2}$ and OER E_{10} values for catalysts modified with different ALD cycles, it is observed that employing 10 cycles of ALD resulted in achieving superior

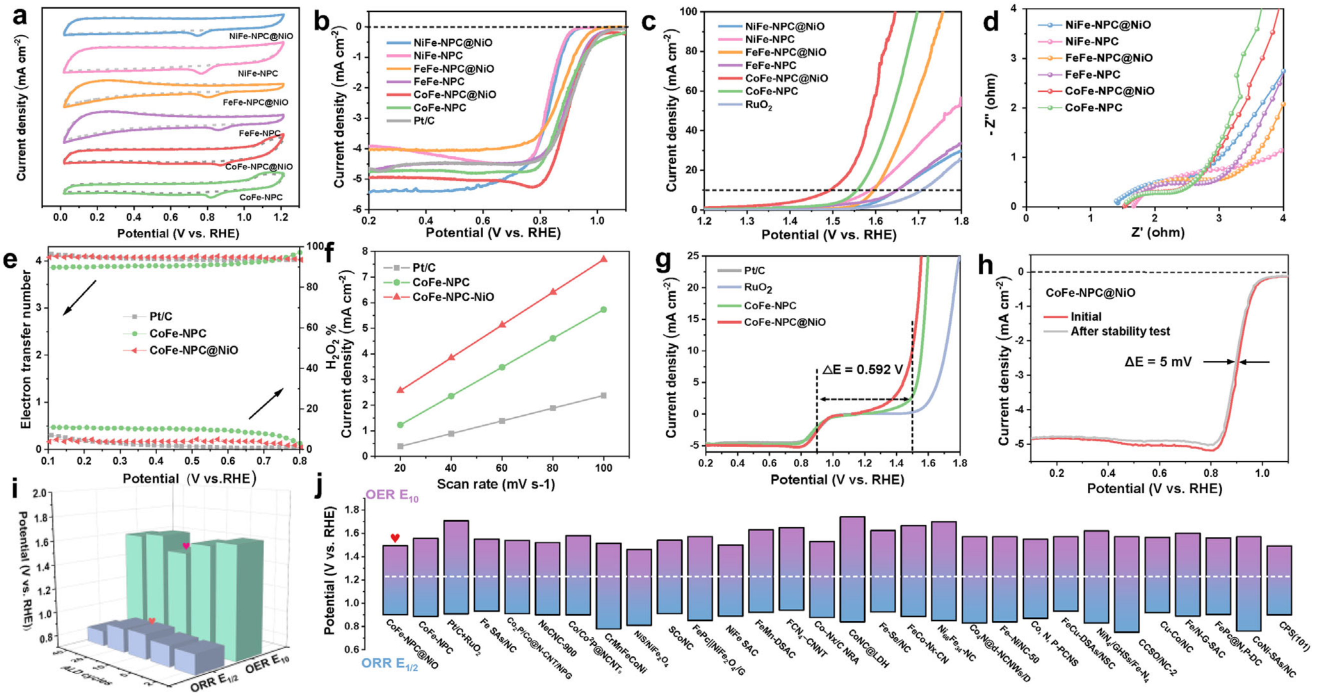

Figure 3. a) CV curves, b) ORR LSV curves, c) OER LSV curves, and d) charge transfer resistance of NiFe-NPC@NiO, NiFe-NPC, FeFe-NPC@NiO, FeFe-NPC, CoFe-NPC@NiO, and CoFe-NPC. e) The electron transfer number (n), H_2O_2 yield, and f) C_{dl} values for Pt/C, CoFe-NPC, and CoFe-NPC@NiO. g) ORR and OER LSV curves of CoFe-NPC, CoFe-NPC@NiO, and Pt/C+RuO_2. h) LSV curves before and after 5000 Cv cycles of CoFe-NPC@NiO. i) Summary of $E_{1/2}$ of ORR and E_{10} of OER for CoFe-NPC@NiO with different ALD cycles. j) Comparison of bifunctional activity for CoFe-NPC, CoFe-NPC@NiO, and recently reported catalysts.

bifunctional activity simultaneously. Moreover, excessively thin or thick ALD coatings exhibit varying degrees of detrimental effects on both ORR and OER.

To gain a deeper understanding of the ORR kinetics of CoFe-NPC@NiO, LSV measurements were performed at various rotational speeds. As the rotational speed increased from 200 to 1600 rpm, the current densities of Pt/C, CoFe-NPC, and CoFe-NPC@NiO showed a gradual increase (Figure S16a–c, Supporting Information). The corresponding Koutecky–Levich (K–L) plot demonstrates a strong linear relationship (Figure S16d–f, Supporting Information), indicating that the ORR follows first-order reaction kinetics with a potential-independent electron transfer rate. The electron transfer number (n) and H_2O_2 yield were determined by using a rotating ring disk electrode (RRDE). The CoFe-NPC@NiO catalyst shows a four-electron transfer ORR pathway, comparable to Pt/C, while achieving a significantly lower H_2O_2 yield (≈4%) compared to CoFe-NPC. This suggests superior selectivity for the desired reaction pathway (Figure 3e). The accelerated reaction kinetics of CoFe-NPC@NiO was further confirmed by its lower Tafel slope (90.76 mV dec^{-1}) compared to COFe-NPC (91.10 mV dec^{-1}) and Pt/C catalyst (103.87 mV dec^{-1}) (Figure S17a, Supporting Information). Furthermore, the effective electrochemically active surface area (ECSA) was evaluated by measuring the double-layer capacitance (C_{dl}) in the non-Faradaic region (Figure S18, Supporting Information). The C_{dl} value for CoFe-NPC@NiO was determined to be 64.02 mF cm^{-2}, higher than that of CoFe-NPC (56.28 mF cm^{-2}) and Pt/C (24.86 mF cm^{-2}), indicating enhanced accessibility of the active sites during electrocatalysis (Figure 3f). As illustrated in Figure 3h, CoFe-NPC@NiO also demonstrated outstanding durability, with only a minimal decay of 5 mV observed after 5000 CV cycles. Chronoamperometric measurements were conducted to evaluate the methanol tolerance of the catalysts. CoFe-NPC@NiO demonstrated the best methanol tolerance, maintaining 95.7% of its initial current after 900 s, closely followed by CoFe-NPC, which retained 92.6% of its initial current. In contrast, the commercial Pt/C catalyst showed a significant decline, with only 48.6% of its initial current remaining (Figure S17b, Supporting Information). In general, the potential difference ΔE between the E_{10} and $E_{1/2}$ is widely acknowledged as a key parameter for evaluating the bifunctional performance of oxygen electrocatalysts. A smaller ΔE value indicates superior bifunctional electrocatalytic activity of the catalyst.[27] The ALD-modified NiO film effectively enhances the bifunctional activity of the CoFe-NPC catalyst, as evidenced by the remarkable decrease in ΔE value depicted in Figure 3g, which surpasses that of commercial Pt/C+RuO_2 catalysts and most advanced catalysts reported to date (Figure 3j; Table S2, Supporting Information).

Considering the exceptional bifunctionality of CoFe-NPC@NiO in the three-electrode system, the construction of ZABs further exemplified its remarkable catalytic activity and stability with zinc plate as the anode, a porous electrode supported by CoFe-NPC@NiO catalyst as the air cathode, and an electrolyte consisting of a mixture of 6.0 M KOH and 0.2 M $Zn(CH_3COO)_2$. Similarly, a comparison was made with a mass ratio of 1:1 Pt/C+RuO_2 assembled ZAB. The CoFe-NPC@NiO-based ZAB, assembled as depicted in **Figure** 4a, illuminates a brilliant blue light-emitting diode (LED) indicator. The ZAB

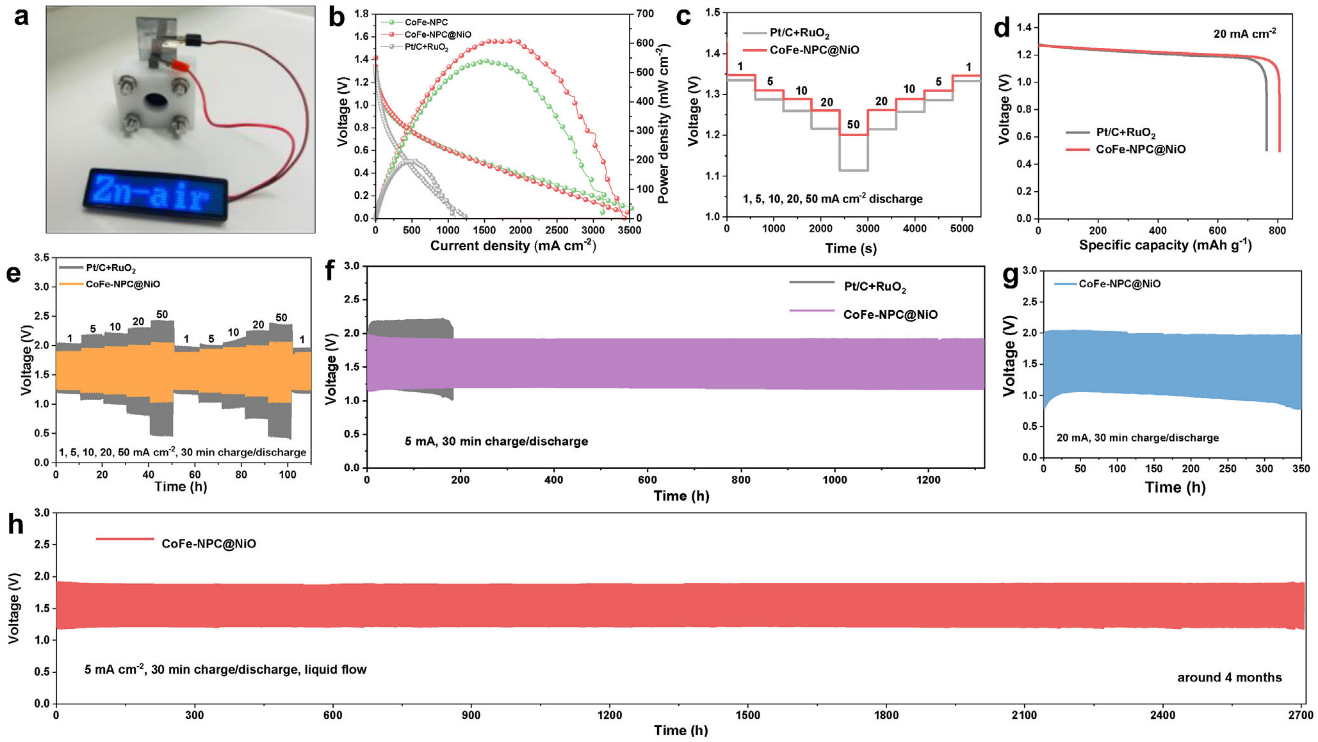

Figure 4. a) Schematic illustration of the assembled ZAB. b) Power density and discharge polarization curves of ZABs using the prepared catalysts. c) Galvanostatic discharge curves under various current densities (1, 5, 10, 20, and 50 mA cm^{-2}), d) specific capacity at 20 mA cm^{-2}, e) galvanostatic charge/discharge cycling at different current densities from 1 to 50 mA cm^{-2}, f) comparison of galvanostatic charge/discharge cycling at 5 mA cm^{-2} of ZABs assembled with Pt/C+RuO_2 and CoFe-NPC@NiO. g) Galvanostatic charge/discharge cycling performance at 20 mA cm^{-2} of CoFe-NPC@NiO-based ZAB. h) Long-term charge/discharge cycling stability of a CoFe-NPC@NiO-based Zn-air flow battery at 5 mA cm^{-2}.

constructed using CoFe-NPC@NiO demonstrates an impressive peak power density of 607 mW cm^{-2}, significantly exceeding that of CoFe-NPC (505 mW cm^{-2}), Pt/C+RuO_2 (195.2 mW cm^{-2}) and other synthetic electrocatalysts including NiFe-NPC, NiFe-NPC@NiO, FeFe-NPC, and FeFe-NPC@NiO (Figure 4b; Figure S19, Supporting Information). Considering potential variations in data due to differences in testing conditions, the maximum peak power density and corresponding current density of recently reported precious metal catalysts are summarized for comparison in Table S3 (Supporting Information).

The galvanostatic discharge performance of ZABs assembled with CoFe-NPC@NiO and Pt/C+RuO_2 catalysts at varying current densities is presented in Figure 4c. The stepped discharge curves indicate a gradual decrease in discharge voltage as the current density increases from 1 to 50 mA cm^{-2}. Notably, the CoFe-NPC@NiO-based ZAB exhibits a significantly higher discharge voltage plateau at each current density compared to the Pt/C+RuO_2 system. Furthermore, when the current density is reduced back to 1 mA cm^{-2} after high-current discharge, the voltage drop in the CoFe-NPC@NiO-based ZAB is negligible, demonstrating exceptional discharge stability and rate performance. The galvanostatic charge–discharge cycling performance at different current densities (1, 5, 10, 20, and 50 mA cm^{-2}) is illustrated in Figure 4e. At each current density, the CoFe-NPC@NiO-based ZAB exhibits a smaller charge-discharge voltage gap compared to the Pt/C+RuO_2-based system. Additionally, the CoFe-NPC@NiO-based ZAB demonstrates more stable charge and discharge voltages, as well as superior reversibility, further confirming its excellent electrochemical performance. The long-term galvanostatic discharge curve at 20 mA cm^{-2} is shown in Figure 4d. By normalizing the weight of zinc consumption, the CoFe-NPC@NiO-based ZAB achieves a specific capacity of 805.96 mAh g^{-1}, surpassing that of the Pt/C + RuO_2 (763.18 mAh g^{-1}). Furthermore, when normalized by the cathode electrode area, the CoFe-NPC@NiO-based ZAB demonstrates a superior aerial capacity of 789.84 mAh cm^{-2} compared to the Pt/C+RuO_2-based ZAB (705.26 mAh cm^{-2}).

The battery's stability was further evaluated at a constant current density of 5 mA cm^{-2} with a cycle period of 1 hour (Figure 4f). In contrast, the Pt/C+RuO_2 ZAB shows a gradual and significant increase in voltage gap, from 0.71 to ≈1.0 V, ultimately leading to rapid failure after limited cyclability (182 h). The performance attenuation is primarily attributed to the decline in catalyst ORR performance, which consequently leads to a reduction in battery discharge efficiency.[28] Figure S20a,b (Supporting Information) shows the SEM images of the CoFe-NPC and CoFe-NPC@NiO catalysts after prolonged charge–discharge cycling, respectively. The images reveal that the initial 3D structures (as shown in Figure 1a,b) of both catalysts collapse due to exposure to the liquid alkaline electrolyte and potential carbon corrosion. However, it is evident that the CoFe-NPC@NiO catalyst (Figure S20b, Supporting Information) retains a more stable porous structure, with much smaller and more uniform nanoparticle sizes, compared to the CoFe-NPC (Figure S20a,

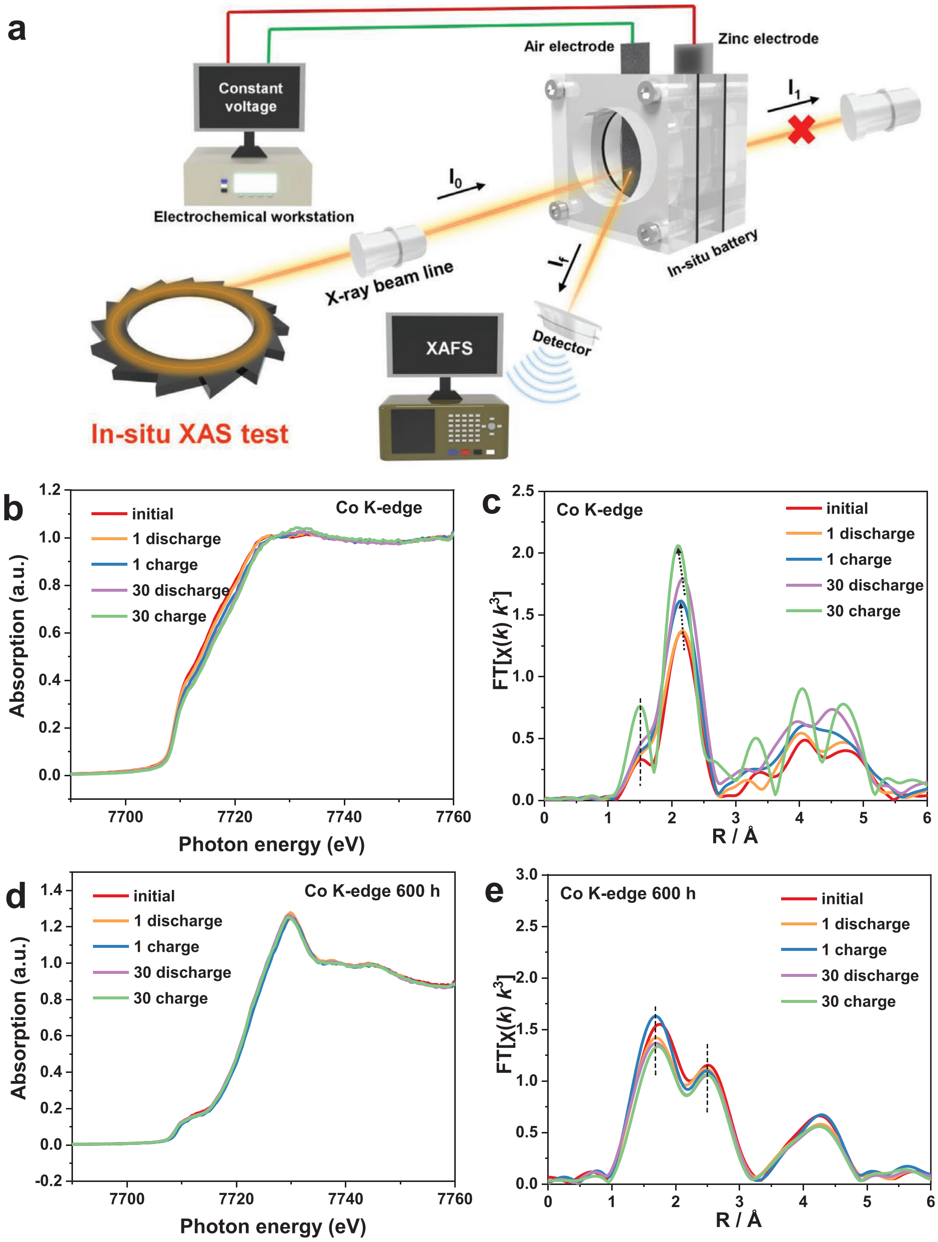

Figure 5. a) Schematic representation of the in situ battery XAS testing setup. In situ Co K-edge XANES spectra and corresponding Fourier transforms of the k^3-weighted EXAFS spectra for b,c) CoFe-NPC@NiO and d,e) CoFe-NPC@NiO-600 h.

Supporting Information). This indicates that the ALD coating of NiO improves the structural stability and carbon corrosion resistance of the catalyst. Moreover, the ZABs employing CoFe-NPC@NiO electrodes display significantly enhanced cycling stability with over 1300 h, compared to CoFe-NPC-based ZABs (560 h) under identical test conditions,[17] accompanied by an exceptionally low voltage decay rate per cycle. Additionally, the charge-discharge voltage difference increases only slightly, from 0.70 to 0.72 V after a total of 1317 h (≈55 days). The CoFe-NPC@NiO ZAB also exhibits excellent stability for 120 h at a high current density of 20 mA cm^{-2}, with minimal voltage attenuation. Furthermore, the battery demonstrated consistent cycling for up to 350 h, resulting in only a marginal increase in the voltage gap by 12 mV (Figure 4g). The ALD-modified NiO coating significantly enhances the stability and performance of the ZAB compared to its unmodified counterpart. Specifically, the CoFe-NPC@NiO ZAB achieves an exceptional cycling duration of 2700 hours (≈113 days) at 5 mA cm^{-2}, surpassing the majority of recently reported catalysts (Figure 4h). These results highlight the long-term stability and practical applicability of the CoFe-NPC@NiO catalyst.

To verify the phase reconstruction of the catalysts, we employed in situ XAS electrochemical cells to conduct in situ XAS analysis at the Co K-edge on CoFe-NPC@NiO and CoFe-NPC@NiO-600 h cathode catalysts (**Figure 5a**). This approach enables direct monitoring of the electrocatalysts' behavior under electrochemical conditions by collecting X-ray absorption spectra during resting, the first, and the 30th discharge–charge cycles. From the Co K-edge XANES spectra shown in Figure 5b, the spectral shape closely resembles that of ex-situ CoFe-NPC@NiO and Co foil. The characteristic absorption edge near 7710 eV gradually shifts to higher energy, suggesting a continuous increase in the oxidation state of Co accompanying the ongoing charge-discharge cycles of the catalyst. It is worth noting that during the 30th discharge process, the edge position shifts markedly toward the right, accompanied by intensity enhancement of the white-line peak.[7b] The in situ EXAFS spectra of CoFe-NPC@NiO are consistent with the results of the ex situ testing, revealing two prominent characteristic peaks corresponding to the Co—O and Co—M coordination (Figure 5c). As the charge-discharge proceeded, the intensity of both characteristic peaks increased. Particularly, there was a slight leftward shift observed in the Co—M peak when discharging occurred. These results confirmed that the Co-active sites in CoFe-NPC@NiO undergo reconstruction accompanying charge and discharge processes in alkaline environments. After 600 h of cycling, the overall spectral shape of the CoFe-NPC@NiO-600 h catalyst exhibits a tendency toward stability, with the discharge and charge spectra essentially overlapping. This observation suggests that Co undergoes reconstruction and maintains a relatively stable state even after multiple charge and discharge cycles. The Co K-edge XANES spectra demonstrate a shift toward higher energies when compared to the ex-situ spectra, which can be attributed to the absorption of dissolved oxygen from the electrolyte on the catalyst surface during electrode immersion.[29] The CoFe-NPC@NiO-600 h shows not only a similar Co-K-Edge XANES spectral shape to CoOOH but also demonstrates the presence of Co—O and Co—Co bonding environments corresponding to CoOOH at distances of 1.7 and 2.50 Å in EXAFS spectrum, respectively (Figure 5d,e). Therefore, from the immersion of CoFe-NPC@NiO-600 h in the electrolyte to the gradual recovery of the charging and discharging process, the Co-active sites in the catalyst gradually stabilize as CoOOH.

It is noteworthy that the relative content of the oxide layer on the surface of CoFe-NPC@NiO-600 h is significantly lower than that of CoFe-NPC@NiO, as indicated by the EXAFS signal. The nearly complete consumption of NiO suggests that the ALD film structure collapses during the charge-discharge cycles (Figure S21, Supporting Information). Despite this, CoFe-NPC@NiO-600 h remains an efficient bifunctional catalyst, capable of sustaining high performance in zinc-air batteries. This observation underscores the potential benefits of additional surface treatments with ALD catalytic active layers to mitigate the oxidation of internal active sites under oxidative conditions, thereby improving the structural stability, catalytic activity, and durability of the bifunctional catalyst.

To elucidate the relationship between the enhanced bifunctional activity/stability and ALD-modified NiO clusters, density functional theory (DFT) calculations were conducted on the optimized model structure. As shown in **Figure 6**a, the simplified geometrical structure of N, P-doped CNTs and the refined configuration of NiO clusters on their surface were optimized for the study. The interaction between O-intermediates and active sites is identified as a key factor influencing the intrinsic catalytic activities for both the ORR and OER. Four fundamental reaction steps for ORR and OER in alkaline media were examined (Figure 6b; Figure S22, Supporting Information). For the ORR, O_2 is initially adsorbed onto the catalyst surface to form OOH*, which is sequentially reduced to O* and then to OH*. In contrast, the O-intermediates undergo oxidation in the reverse sequence during the OER process. Computational analysis reveals that the oxygen adsorption energy on both CoFe-NPC and CoFe-NPC@NiO surfaces is negative, indicating thermodynamically favorable interactions between oxygen molecules and the catalyst surface (Figure 6c; Figure S23, Supporting Information). Notably, the oxygen adsorption energy on CoFe-NPC@NiO (−2.147 eV) is significantly more negative than that for CoFe-NPC (-1.612 eV). This suggests a stronger oxygen affinity for the CoFe-NPC@NiO surface, a critical factor for initiating the ORR and enhancing overall reaction kinetics. The enhanced oxygen affinity can be attributed to the NiO clusters, which provide additional active sites capable of forming strong bonds with oxygen molecules, thereby reducing system energy. Moreover, the charge transfer between the NiO clusters and the N, P-doped CNTs alters the electronic structure of the catalyst surface. This electronic modification enhances the adsorption capacity for oxygen intermediates, thereby improving the bifunctional catalytic performance.

We investigated the adsorption behavior of O-intermediates at active sites during the ORR and OER, which is illustrated through the free energy diagrams for both reactions on CoFe-NPC and CoFe-NPC@NiO at applied potentials of U = 0 V and U = 1.23 V. At U = 0 V, all ORR steps on both CoFe-NPC and CoFe-NPC@NiO exhibit a consistent decrease in free energy, indicating that these intermediate reactions are energetically favorable (Figure 6d). However, at the equilibrium potential of U = 1.23 V, a significant shift in the free energy trend is observed. For CoFe-NPC@NiO, the free energy increases during the formation of *OOH and then gradually decreases during the later process. In contrast, CoFe-NPC demonstrates a more complex behavior, characterized by an upward, downward, and then upward trend in the formation stages of *OOH, *O, and *OH, respectively. The maximum free energy change (ΔG) for CoFe-NPC@NiO and CoFe-NPC is 0.707 and 0.956 eV, indicating that the rate-determining step (RDS) is the *OOH intermediate formation stage and the *OH formation from *O, respectively. The lower energy barrier in the CoFe-NPC@NiO system reflects a synergistic effect between the NiO nanoclusters and N, P-doped CNTs, which enhances ORR activity by facilitating intermediate formation and reaction kinetics. For the OER at U = 0 V, the respective ΔG values for each elementary step on CoFe-NPC@NiO are 1.296, 1.676, 1.452, and 0.532 eV, respectively (Figure 6e). The largest barrier appears in the step involving the conversion of *OH to *O, identifying it as the RDS. In contrast, for CoFe-NPC, the formation of OOH* exhibits the largest free energy change, establishing this step as the RDS. At U = 1.23 V, the RDS for both CoFe-NPC@NiO and CoFe-NPC remains the conversion from *OH to *O and the formation of OOH*, respectively. However, the ΔG associated with the RDS is lower for CoFe-NPC@NiO compared to CoFe-NPC. This reduction in the energy barrier suggests that the NiO clusters not only enhance the formation of OER intermediates but also improve the overall reaction kinetics.

The binding energy of NiO clusters on N/P-doped CNTs was calculated to be -5.74 eV, indicating stable adsorption on the N, P-CNT surfaces. This negative binding energy reflects the strong

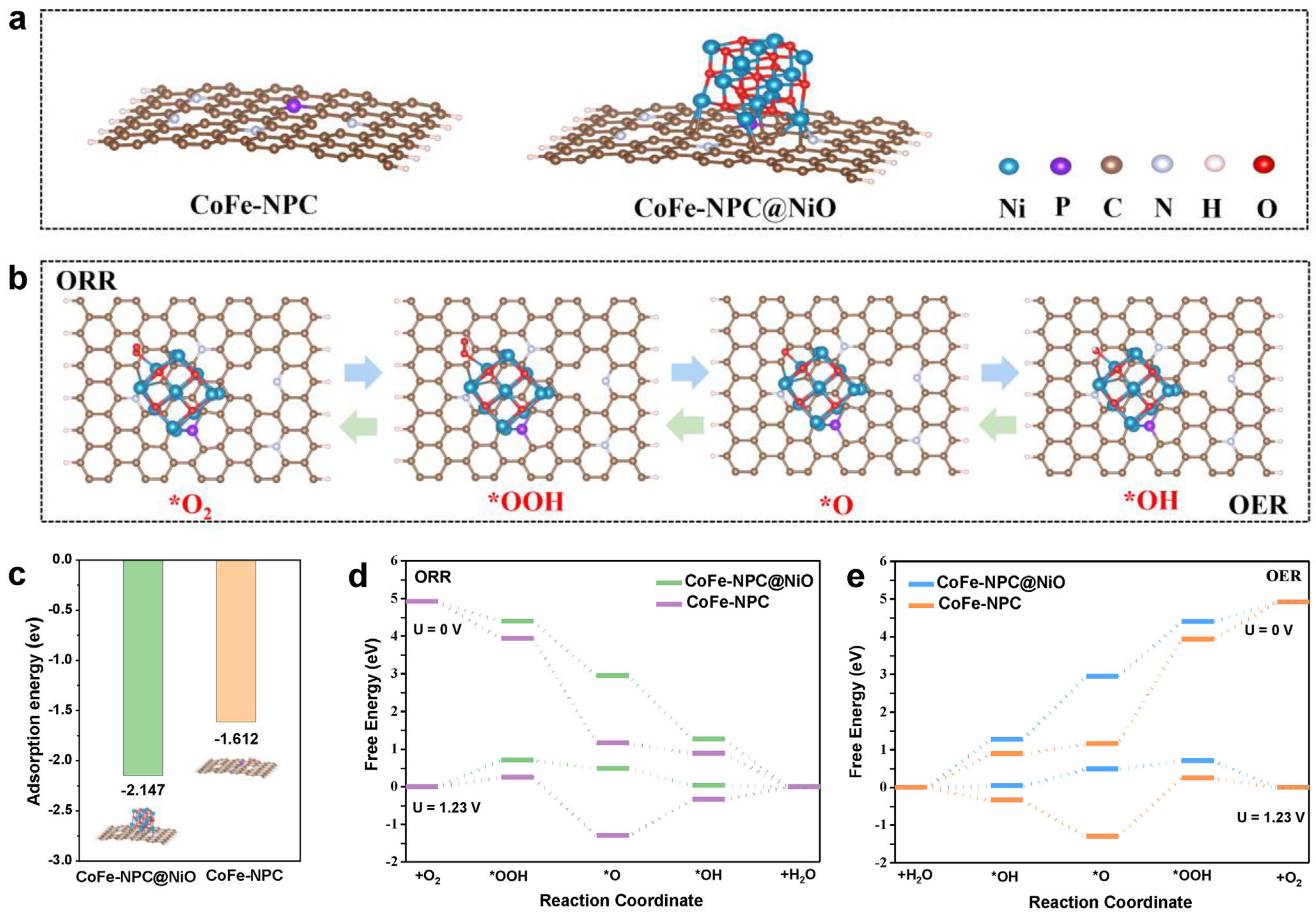

Figure 6. a) Optimized model configurations of CoFe-NPC and CoFe-NPC@NiO. Blue, purple, brown, silver, rose gold, and red spheres represent Ni, P, C, N, H, and O atoms, respectively. b) Schematic illustration of the reaction mechanisms for the ORR and OER processes on the CoFe-NPC@NiO surface in an alkaline medium. c) Adsorption energies of O_2 on CoFe-NPC and CoFe-NPC@NiO surfaces. Free energy profiles for d) ORR and e) OER processes on CoFe-NPC and CoFe-NPC@NiO surfaces at U = 0 V and U = 1.23 V.

interaction between the NiO clusters and the doped CNTs, contributing to excellent structural stability. Such stability is essential for inhibiting catalyst corrosion and preserving the material's integrity in the electrolyte, thereby ensuring a prolonged service life during battery charge-discharge cycles.

3. Conclusion

In summary, the ALD-modified NiO coating on the CoFe-NPC catalyst not only functions as an additional catalytically active component but also effectively mitigates electrocatalyst corrosion. Benefiting from the modified electronic structure and the well-designed architecture, the CoFe-NPC@NiO catalyst exhibits outstanding bifunctional performance ($\Delta E = 0.592$ V), surpassing both precious metal-based electrocatalysts and most advanced bifunctional catalysts. When the CoFe-NPC@NiO catalyst is incorporated into the air electrode, the rechargeable ZAB demonstrates exceptional long-term stability, maintaining performance for over 2700 h at 5.0 mA cm^{-2}. In situ, XAS analysis reveals the dynamic reconfiguration and evolutionary maturation of the catalyst during ZAB operation. Simulations further confirm that NiO clusters significantly enhance the bifunctional activity and stability by modulating the electronic structure and optimizing the adsorption of key reaction intermediates, aligning well with experimental findings. The controlled reconfiguration promotes the formation of an efficient and stable electrocatalyst, preserving its original structure and preventing corrosion. This advancement is pivotal for achieving continuous and efficient energy conversion in ZABs.

Supporting Information

Supporting Information is available from the Wiley Online Library or from the author.

Acknowledgements

This work was supported by the Natural Sciences and Engineering Research Council of Canada (NSERC), Fonds de Recherche du Québec-Nature et Technologies (FRQNT), Centre Québécois sur les Materiaux Fonctionnels (CQMF, https://doi.org/10.69777/341666), École de Technologie Supérieure (ÉTS), and Institut National de la Recherche Scientifique (INRS). F.D. acknowledges scholarships from FRQNT and the CLS Student Travel Support Program. Prof. G. Zhang thanks for the support from the Marcelle-Gauvreau Engineering Research Chair program, and the Canada Research Chair Programs.

Conflict of Interest

The authors declare no conflict of interest.

Data Availability Statement

The data that support the findings of this study are available in the supplementary material of this article.

Keywords

atomic layer deposition, bifunctional electrocatalysts, in situ observation, zinc-air batteries

Received: April 12, 2025
Published online:

[1] a) Y. Wang, J. Wu, S. Tang, J. Yang, C. Ye, J. Chen, Y. Lei, D. Wang, *Angew. Chem. Int. Ed. Engl.* **2023**, *62*, 202219191; b) X. Shu, Q. Chen, M. Yang, M. Liu, J. Ma, J. Zhang, *Adv. Energy Mater.* **2022**, *13*, 2202871.

[2] a) Z. Hou, Z. Sun, C. Cui, D. Zhu, Y. Yang, T. Zhang, *Adv. Funct. Mater.* **2022**, *32*, 2110572; b) Y. Dou, S. Xing, Z. Zhang, Z. Zhou, *Electrochem. Energy Rev.* **2024**, *7*, 6; c) W. Shao, R. Yan, M. Zhou, L. Ma, C. Roth, T. Ma, S. Cao, C. Cheng, B. Yin, S. Li, *Electrochem. Energy Rev.* **2023**, *6*, 11.

[3] a) F. Dong, C. Liu, M. Wu, J. Guo, K. Li, J. Qiao, *ACS Sustainable Chem. Eng.* **2019**, *7*, 8587; b) W. Ou, X. Ye, Y. Zhou, *Coord. Chem. Rev.* **2023**, 493. https://doi.org/10.1016/j.ccr.2023.215274.

[4] a) B. Wu, T. Sun, Y. You, H. Meng, D. M. Morales, M. Lounasvuori, A. B. Askari, L. Jiang, F. Zeng, B. Hu, R. Tai, J. X. Z., T. Petit, L. Mai, *Angew. Chem. Int. Ed. Engl.* **2023**, *135*, 202219188; b) F. Dong, M. Wu, G. Zhang, X. Liu, D. Rawach, A. C. Tavares, S. Sun, *Chem. Asian J.* **2020**, *15*, 3737.

[5] a) Z. Shao, Q. Zhu, Y. Sun, Y. Zhang, Y. Jiang, S. Deng, W. Zhang, K. Huang, S. Feng, *Adv. Mater.* **2022**, *34*, 2110172; b) M. Wu, F. Dong, Y. Yang, X. Cui, X. Liu, Y. Zhu, D. Li, S. Omanovic, S. Sun, G. Zhang, *Electrochem. Energy Rev.* **2024**, *7*, 10; c) M. Du, B. Chu, Q. Wang, C. Li, Y. Lu, Z. Zhang, X. Xiao, C. Q. Xu, M. Gu, J. Li, H. Pang, Q. Xu, *Adv. Mater.* **2024**, *36*, 2412978.

[6] a) L. Li, H. Sun, Z. Hu, J. Zhou, Y. C. Huang, H. Huang, S. Song, C. W. Pao, Y. C. Chang, A. C. Komarek, H. J. Lin, C. T. Chen, C. L. Dong, J. Q. Wang, L. Zhang, *Adv. Funct. Mater.* **2021**, *31*, 2104746; b) F. Dong, M. Wu, Z. Chen, X. Liu, G. Zhang, J. Qiao, S. Sun, *Nano-Micro Lett.* **2021**, *14*, 36; c) M. Xie, Y. Lu, X. Xiao, D. Wu, B. Shao, H. Nian, C. Wu, W. Wang, J. Gu, S. Han, M. Gu, Q. Xu, *Adv. Funct. Mater.* **2024**, 35. https://doi.org/10.1002/adfm.202414537.

[7] a) F..-M. Li, C. Xia, B. Y. Xia, *Acc. Mater. Res.* **2023**, *4*, 427; b) Y. P. Deng, Y. Jiang, R. Liang, S. J. Zhang, D. Luo, Y. Hu, X. Wang, J. T. Li, A. Yu, Z. Chen, *Nat. Commun.* **2020**, *11*, 1952.

[8] a) H. Yang, Y. Chen, Y. Qin, *Chinese J. Catal.* **2020**, *41*, 227; b) Z. Li, J. Su, X. Wang, *Carbon* **2021**, *179*, 299.

[9] a) S. Moller, S. Barwe, J. Masa, D. Wintrich, S. Seisel, H. Baltruschat, W. Schuhmann, *Angew. Chem. Int. Ed. Engl.* **2020**, *59*, 1585; b) S. Zago, L. C. Scarpetta-Pizo, J. H. Zagal, S. Specchia, *Electrochem. Energy Rev.* **2024**, *7*, 1.

[10] a) F. M. Li, L. Huang, S. Zaman, W. Guo, H. Liu, X. Guo, B. Y. Xia, *Adv. Mater.* **2022**, *34*, 2200840; b) Y. Cheng, H. Wang, T. Qian, C. Yan, *EnergyChem.* **2022**, 4, https://doi.org/10.1016/j.enchem.2022.100074.

[11] a) F. Dong, Y. Cai, C. Liu, J. Liu, J. Qiao, *Int. J. Hydrog. Energy* **2018**, *43*, 12661; b) C. Liu, F. Dong, Y. Wang, J. Guo, Y. Yang, Q. Gong, J. Qiao, *Int. J. Hydrogen Energy* **2019**, *45*, 29874; c) X. Pu, S. Zhang, D. Zhao, Z.-L. Xu, Z. Chen, Y. Cao, *Electrochem. Energy Rev.* **2024**, *7*, 21.

[12] L. Lei, F. Li, X. Jiang, H. Yang, B. Y.u Xia, *Adv. Funct. Mater.* **2024**, *34*, 2405726.

[13] a) N. C. Paranamana, R. Gettler, H. Koenig, S. Montgomery-Smith, X. He, M. J. Young, *ACS Appl. Nano Mater.* **2022**, *5*, 12582; b) S. Yan, H. Li, J. Zhu, W. Xiong, R. Lei, X. Wang, *Nanotechnology* **2021**, *32*, 275402.

[14] Y. Zhao, L. Zhang, J. Liu, K. Adair, F. Zhao, Y. Sun, T. Wu, X. Bi, K. Amine, J. Lu, X. Sun, *Chem. Soc. Rev.* **2021**, *50*, 3889.

[15] R. M. Silva, J. Rocha, R. F. Silva, *Nanoscale* **2023**, *15*, 10423.

[16] a) K. L. Pickrahn, S. W. Park, Y. Gorlin, H.-B.-R. Lee, T. F. Jaramillo, S. F. Bent, *Adv. Energy Mater.* **2012**, *2*, 1269; b) H. Li, Z. Guo, X. Wang, *J. Mater. Chem. A* **2017**, *5*, 21353; c) Z. Zhao, Y. Kong, Z. Zhang, G. Huang, Y. Mei, *J. Mater. Res.* **2019**, *35*, 701.

[17] F. Dong, M. Wu, Z. Chen, N. Chen, M. Bakhtbidar, A. Ruediger, G. Zhang, S. Sun, *Nano Energy* **2025**, *133*, 110497.

[18] a) L. Peng, J. Yang, Y. Yang, F. Qian, Q. Wang, D. Sun-Waterhouse, L. Shang, T. Zhang, G. I. N. Waterhouse, *Adv. Mater.* **2022**, *34*, 2202544; b) S. H. Lee, J. Kim, D. Y. Chung, J. M. Yoo, H. S. Lee, M. J. Kim, B. S. Mun, S. G. Kwon, Y. E. Sung, T. Hyeon, *J. Am. Chem. Soc.* **2019**, *141*, 2035.

[19] a) S. Liang, L. C. Zou, L. J. Zheng, F. Li, X. X. Wang, L. N. Song, J. J. Xu, *Adv. Energy Mater.* **2022**, *12*, 2103097; b) M. Fan, Q. Yuan, Y. Zhao, Z. Wang, A. Wang, Y. Liu, K. Sun, J. Wu, L. Wang, J. Jiang, *Adv. Mater.* **2022**, *34*, 2107040; c) Y. Jiang, Y. P. Deng, R. Liang, J. Fu, R. Gao, D. Luo, Z. Bai, Y. Hu, A. Yu, Z. Chen, *Nat. Commun.* **2020**, *11*, 5858; d) J. Qin, Z. Yang, F. Xing, L. Zhang, H. Zhang, Z..-S. Wu, *Electrochem. Energy Rev.* **2023**, *6*, 9.

[20] N. Wang, D. Chen, S. Ning, J. Lao, J. Xu, M. Luo, W. Zhang, J. Chen, M. Yang, F. Xie, Y. Jin, S. Sun, H. Meng, *Adv. Mater.* **2024**, *36*, 2306138.

[21] a) H. Chang, X. Liu, S. Zhao, Z. Liu, R. Lv, Q. Zhang, T. F. Yi, *Adv. Funct. Mater.* **2023**, *34*, 2313491; b) H. W. Go, T. T. Nguyen, Q. P. Ngo, R. Chu, N. H. Kim, J. H. Lee, *Small* **2023**, *19*, 2206341.

[22] Y. Chen, S. Qiao, Y. Tang, Y. Du, D. Zhang, W. Wang, H. Zhang, X. Sun, C. Liu, *ACS Nano* **2022**, *16*, 15273.

[23] R. S. Kumar, P. Mannu, S. Prabhakaran, T. T. T. Nga, Y. Kim, D. H. Kim, J. L. Chen, C. L. Dong, D. J. Yoo, *Adv. Sci.* **2023**, *10*, 2303525.

[24] M. B. Stevens, L. J. Enman, E. H. Korkus, J. Zaffran, C. D. M. Trang, J. Asbury, M. G. Kast, M. C. Toroker, S. W. Boettcher, *Nano Res.* **2019**, *12*, 2288.

[25] M. Lee, W. Ahmad, D. W. Kim, K. M. Kwon, H. Y. Kwon, H.-B. Jang, S.-W. Noh, D.-H. Kim, S. J. A. Zaidi, H. Park, H. C. Lee, M. Abdul Basit, T. J. Park, *Chem. Mater.* **2022**, *34*, 3539.

[26] J. Lu, J. W. Elam, P. C. Stair, *Surf. Sci. Rep.* **2016**, *71*, 410.

[27] Z. Li, S. Ji, C. Xu, L. Leng, H. Liu, J. H. Horton, L. Du, J. Gao, C. He, X. Qi, Q. Xu, J. Zhu, *Adv. Mater.* **2023**, *35*, 2209644.

[28] Q. Liu, Y. Wang, L. Dai, J. Yao, *Adv. Mater.* **2016**, *28*, 3000.

[29] F. Jiang, F. Zhu, F. Yang, X. Yan, A. Wu, L. Luo, X. Li, J. Zhang, *ACS Catal.* **2019**, *10*, 604.